

Contents list available at IJRED website

IS INTERPOLATION SET OF A PARTIES AND SET OF SET O

Journal homepage: https://ijred.undip.ac.id



Research Article

Numerical modelling and experimental assessment of cap magnet motion in a small windbelt generator

Thi Tuyet Nhung Lea* 📵 , Dinh Quy Vu 👊 , Cong Truong Dinh 🕫 , Duc Trung Nguyen a, Frederic Plourdeb

^aSchool of Mechanical Engineering, Hanoi University of Science and Technology, 1 Dai Co Viet, Hanoi, Vietnam ^bENSMA, INSTITUT P', UPR 3346, 1 avenue Clément Ader, BP 40109, 86961 Futuroscope Chasseneuil Cedex, France

Abstract. Wind energy shows great potential as a power source for low-energy electronics. A promising innovation in this field is a compact generator based on electromagnetic induction and oscillation, designed with simplicity and efficiency in mind. Small wind-driven generators utilize membrane oscillations and electromagnetic induction to produce voltages of a few volts, offering a potential future alternative to batteries due to their portability and easy power supply. This study focuses on evaluating the parameters that affect the voltage and power output of a small belt-type generator with a maximum wire length of 350 mm, operating at low wind speeds ranging from 2.5 to 6 m/s. The influence of wire length is examined to assess power and voltage output using the shortest practical wire length. Additionally, the effects of membrane oscillation amplitude and the number of coils turns in the electromagnetic setup are also investigated. Two methods were employed in this study: two-way FSI simulations method and experimental tests measuring membrane oscillation, voltage, and power output. Key findings include a 9% error between experimental and simulated oscillation amplitude and a 12% difference between theoretical and experimental voltage results. The oscillation amplitude gradually decreased as the wire length was reduced from 350 mm to 198 mm, with corresponding slight decreases in voltage and power. For the 350 mm wire, the maximum no-load voltage reached 8V and 0.8V under a $1 k\Omega$ load; for the shortest wire of 198 mm, the no-load voltage reached 7.5V, but the power output under load was minimal.

Keywords: Windbelt, Experiment, FSI Simulation, Aeroelasticity, Vibration Amplitude.



@ The author(s). Published by CBIORE. This is an open access article under the CC BY-SA license (http://creativecommons.org/licenses/by-sa/4.0/).

Received: 5th January 2025; Revised: 6th March 2025; Accepted: 15th March 2025; Available online: 26th March 2025

1. Introduction

These days, low-power electronic gadgets are being developed and made more widely available. Examples include wireless sensors and mobile phones. These devices run on batteries, which provide significant issues for both users and the environment due to their short lifespan and the need for replacement or further charging. As a result, using renewable energy sources, like wind energy, to provide energy seems like a feasible answer. Since their invention in 1887, wind power production devices, such as wind turbines, have produced vast amounts of energy. However, their massive structure and high construction costs make them unsuitable for small-capacity devices.

The windbelt, a device invented by Shawn Frayne (Shawn, 2004), with its simple design, generates energy based on electromagnetic induction. With a long wire structure and a pair of magnets, it relies on wind energy to create a self-exciting vibration phenomenon that changes the magnetic field through two copper coils and generates small currents suitable for small power devices. These small-scale generator devices can be based on three fundamental working principles: using piezoelectric, electrostatic, or electromagnetic transducers. Table 1 presents a review of several studies based on these three types of transducers.

Numerous studies have explored small-scale generators aimed at analyzing oscillatory behavior that contributes to capacitance build-up in membranes, enabling the generation of usable voltage while maximizing strain energy and ensuring structural durability. These investigations often combine turbulent flow fields with oscillating membrane dynamics, as seen in the works of (Allen et al., 2000), (Abdehvand et al., 2020), (Kurhade et al., 2017), and (Bae et al., 2014). A charged beam with a D-shaped cross-section and a rigid tip mass was utilized by (Sirohi et al., 2011) to harness wind energy. The top and bottom surfaces of the beam are covered with bonded piezoelectric sheets. During galloping, aerodynamic forces on the D-section induce vibrational motion, which is then converted into electrical energy via the piezoelectric material. Similarly, (Li et al., 2011) proposed and tested a bio-inspired piezo-leaf design that converts wind-induced flapping into electrical energy. Unlike traditional flutter-based devices positioned parallel to the flow, Li's design employs a hanging crossflow stalk configuration, offering a novel approach to wind energy harvesting.

Likewise, in 2010, Erturk and colleagues (Erturk *et al.*, 2010) investigated piezo aeroelasticity for energy harvesting, emphasizing both mathematical modeling and experimental validation of electricity generation at the flutter boundary of a piezo-aeroelastic airfoil. A power output of 10.7 mW was

Table 1

delivered to a 100 k Ω load at a flutter speed of 9.30 m/s. In another study, Bangi and colleagues (Bangi *et al.*, 2017) examined the feasibility of electricity generation using a pair of micro-wind turbines and two micro-generators mounted on the rear of a car trunk. The impact of drag force on vehicle performance was evaluated through both computational fluid dynamics (CFD) simulations and experimental analysis. A maximum voltage of 18.91 V and a peak current of 0.65 A were recorded when six flash bulbs were connected in series.

The study by Ali *et al.*, (2024) provides a comprehensive review of piezoelectric materials used in energy harvesting and examines various design strategies for wind energy harvesters. In a related investigation, Fei *et al.*, (2012) employed the flutter principle to generate approximately 7 mW of electrical power at a wind speed of around 3 m/s using a 1-meter-long belt. Similarly, Lu *et al.*, (2019) designed an optimized wind energy harvester capable of producing a maximum average power output of 705 W at a wind speed of 10 m/s.

Buyukkseskin et al., (2019) investigated moderate and strong turbulent flows at various wind speeds using circular and fourcornered wind stalk structures. A power density of 380.73 W/cm2 was achieved at a wind speed of 17 m/s. Lang et al., (2025) conducted wind tunnel experiments to examine aerodynamic interactions and vortex-induced vibration (VIV) characteristics in a tandem arrangement of circular cylinders equipped with end plates. Additionally, extensive research has focused on small windbelt generators. Preliminary theoretical formulas for calculating voltage and capacitance based on the windbelt's magnetic field, oscillation frequency, and amplitude have been proposed (Tathode et al., 2017). Experimental studies have also explored the input parameters affecting the output voltage and power of windbelts, such as wire tension, wind speed, and wire length (Vu et al., 2016; Vinayan et al., 2019). Le et al., (2023) experimentally measured voltage and membrane oscillation amplitude in subsonic wind tunnels, observing an increase in voltage from 4 V to 11.41 V as wire length varied between 540 mm and 620 mm at wind speeds of 1.93 to 3.93 m/s. Some studies have harnessed the flutter phenomenon in combination with the triboelectric effect to generate electricity. For example, (Bae et al., 2014) developed a compact generator measuring 7.5×5 cm, capable of producing an output voltage of 200 V, a current of 60 mA, and an average power of 0.86 mW. (Phan et al., 2017) demonstrated that a single flutter-membranebased triboelectric nanogenerator (FM-TENG) could produce

up to $0.33~\mu W$ of triboelectric power under gentle airflow. Table 1 provides a summary of the experimental studies on ultra-small generators based on the flutter mechanism. Many of these generators utilize piezoelectric materials as transducers and are primarily designed for small-scale applications, with output power ranging from 0.4~mW to 120~mW. The generated power is largely influenced by the type of semiconductor material employed. Generators based on electromagnetic transduction principles were extensively examined by Angelo *et al.*, (2017), who focused on external flow conditions and optimal placement for maximizing power output. However, this study did not address the dimensions of the belt membrane.

The windbelt generator device was developed in a study on stretched ribbon fabric and can achieve a power output of 171 mW at a wind speed of 20 m/s (Pimenter *et al.*, 2010). Another study proposed designing optimization of a wind belt generator employing piezoelectric transducers to supply power to lowenergy devices (Fernandez *et al.*, 2018). By combining both electromagnetic and piezoelectric principles, the author achieved a maximum voltage of 8.2 V.

In the study of (Vu et al., 2016), the authors based their investigation on a belt membrane size of 350 mm x 10 mm, examining parameters that affect the generator's power output. The results indicated that with a belt length of 350 mm, the device can reach a maximum power output of 3 mW and 2.5 V at a wind speed of 6 m/s. To create a reference range for power output based on belt length, (Le et al., 2023) expanded the study to include a broader range of belt lengths, from 540 mm to 620 mm. Their findings revealed that, in this instance, the voltage could reach as high as 11.41 V, accompanied by a power output of 0.39 mW at a speed of 1.93 m/s. This suggests that for applications utilizing the flutter-electromagnetic principle, such as sensor enclosures on utility poles, belt lengths under 350 mm have not yet been studied.

In addition to experimental studies, a current research trend emphasizes simulating the oscillations of small generators using numerical methods. Simulating membrane oscillations under varying wind conditions offers a cost-effective and time-efficient means of estimating power and voltage output (Angelo *et al.*, 2017). However, no existing study has applied two-way fluid-structure interaction (FSI) methods to determine optimal operating conditions by analyzing membrane oscillation patterns and amplitudes over time. Based on the summary in Table 1, this study aims to clarify the impact of belt membrane

Overview of the technical features of wind-induced vibration generators utilizing flutter

Author	tures of wind-induced vibration gen Body shape	Power capacity	Transducer
De Sousa et al. 2015	Aerofoil	120mW at 14 m/s	Piezoelectric
Zhang et al. 2015	Cuboid shape and cantiliverbeam	1.59 mW at $20 \text{k}\Omega$ and 11.2 m/s ,	Piezoelectric
Shan <i>et al</i> . 2020	Aerofoil	0.764mW, 17.48V at 16.32 m/s	Piezoelectric
Sirohi 2012	PZT sheet	1.14 mW at 4.69 m/s	Piezoelectric
Shuguang 2011	Crossflow stalk leaf	0.61 mW at 4m/s	Piezoelectric
Erturk et al. 2010	Aerofoil	10.7 mW at 100kΩ and 9.3m/s	Piezoelectric
Büyükkeskin 2019	Base and stalk	380.73 µW/cm2 at 17 m/s	Piezoelectric
Perez et al. 2015	Teflon electret layer	481 µW at 15 m/s, 2.1 mW at 30 m/s	Electrostatic
Shawn 2004	Belts (LxW)	40 mW in 10-mph	Electromagnetic
Pimentel <i>et al.</i> 2010 Fernandez <i>et al.</i> 2018	Belts (LxW) (0.5x0.052) Belts (LxW) (0.75x0.005)	171mW at 110Ω and 20m/s 8.2 V	Electromagnetic Electromagnetic
Vu et al. 2016	Belts (LxW) 0.35m x 0.01m	3mW, 2.5V, 0.5 mA at 6 m/s	Electromagnetic
Angelo et al. 2017	aeroelastic belts	62.4 mW with v=6.2 m/s	Electromagnetic
Angelo et al. 2017	aeroelastic belts	8.72V, 1mA at v=2.3 m/s	Electromagnetic
Le et al. 2023	windbelts (LxW) 0.62m x 0.02m	0.39mW, 11.4 V, at 3.93 m/s	Electromagnetic

oscillations on generator power and voltage output by employing two-way FSI simulations alongside experimental measurements of membrane oscillation amplitude to analyze this influence mechanism in greater detail.

The membrane's oscillating wave was modeled using a twoway FSI (fluid-structure interaction) simulation approach. This technique has been widely studied, particularly in the context of NASA's AGARD wing. In 2003, multiple simulations were conducted to validate and compare AGARD wing data at Mach 0.338 with experimental results from (Yates et al., 1963), (Yates and Carson, 1987), and (Slone et al., 2003). Additionally, (Başkut et al., 2012) performed simulations to compute the Flutter Speed Index across various Mach number scenarios and proposed a method for determining time steps in aeroelastic simulations. Keshavarzi (Keshavarzi et al., 2016) further investigated how mesh modifications influence aeroelastic simulation outcomes. Fabien Salmon (Salmon et al., 2021) also demonstrated that multiple parameters-including mesh quality-affect the accuracy of two-way FSI simulations, particularly in studies on the aeroelastic behavior of hydrofoils at low Reynolds numbers.

In addition, FSI simulations require the simultaneous application of computational fluid dynamics (CFD) and computational structural dynamics (CSD) methods. While small-scale wind turbines are widely investigated using CFD techniques, FSI has been utilized in relatively few studies. (Wu et al., 2022) conducted a comprehensive review of recent CFD research focused on micro and small wind turbines, including those integrated with buildings. Their findings highlight CFD's effectiveness in predicting and optimizing turbine performance, though challenges remain in modeling complex turbulent flows. The review underscores CFD's potential to reduce design costs, enhance turbine efficiency, and improve wind energy utilization, particularly in urban environments.

Similarly, (Heo *et al.*, 2016) used CFD to analyze the aerodynamic performance of a 110-kW building-augmented wind turbine (BAWT). The study examined wind speed and flow angles within atmospheric boundary layers and found that wind speeds increased axially between buildings due to flow separation at sharp corners. As a result, the BAWT generated greater aerodynamic power than a standalone turbine of the same capacity, benefiting from the wind acceleration and concentration effect between structures.

(Chawdhury et al., 2018) incorporated a cantilever beam into their energy harvester design and assessed aeroelastic instabilities and flutter using FSI simulations. A CFD solver based on the vortex particle method (VPM) was employed to study the behavior of a T-shaped cantilever beam in small-scale wind energy harvesting. The CFD results closely matched wind tunnel data, with consistent energy output and flutter speed across varying electrical resistances. The system achieved a maximum power output of 5.3 mW at a wind speed of 8 m/s.

FSI simulation is an effective method for pre-characterizing the performance parameters of windbelt generators. In this study, membrane oscillations under various wind speeds were analyzed using two-way FSI simulations in conjunction with experimental validation. The primary aim of this research is to develop compact generators under 300 mm in length, assessing their potential voltage and power output for sensor box applications. Given the limited size of sensor enclosures—typically under 30 cm—the study investigates belt lengths ranging from 350 mm down to 200 mm, focusing on the shortest feasible dimensions capable of harnessing aeroelastic flutter for energy generation. Since the generator's power output is directly linked to the oscillation of the belt membrane, controlling and predicting oscillation amplitude allows for

theoretical power estimation. This amplitude can be determined experimentally or through two-way fluid-structure interaction (FSI) simulations. A secondary objective of the study is to use simulated membrane oscillation amplitudes to predict the generator's theoretical voltage output.

2. Material and method

2.1 Theoretical principles of windbelt

A windbelt includes four principal components: coil, cap magnet, membrane, and frame. The size of the windbelt is 390x280x200 mm which is suitable for placing in the subsonic wind tunnel with a test section of 400 x 400 mm. The frame, 390mm long, is made of ABS plastic material by using 3D printing. The belt base is drilled with pairs of holes 20 mm apart so that the position of the belt mount can be easily changed. This makes a difference in altering the length of the belt for the test process. A ripstop nylon fabric membrane 350mm long and 0.25 mm thick is fixed in the two ends of the frame. In this study, 2 copper coils of 0.18 mm diameter with the number of rounds from 2500 to 4000 are utilized. Two cap magnets are placed on two faces of the membrane. Components are linked together by bolts and screws. An illustration of a 350mm windbelt model is shown in Figure 1.

The working principle of this generator is based on the oscillation of the magnet placed between two coils. Due to the variation of the magnetic field in the coils, an electric current is generated. The power generated can be theoretically calculated as follows (Tathode *et al.*, 2017):

$$P=U.I$$
 (1)

$$U=2\pi NfA_cB \tag{2}$$

$$f=v/d$$
 (3)

$$A_c=L.b$$
 (4)

$$B = \frac{B_r}{2} \left(\frac{D+z}{\sqrt{R^2 + (D+z)^2}} - \frac{z}{\sqrt{R^2 + z^2}} \right)$$
 (5)

where:

• P : Power of generator (mW)

• I : current (mA)

U : Voltage generated (V)
N : Number of cycles of coil
A_c : Area of the membrane (m2)
B : Magnetic field intensity (Tesla)

• F : frequency of flutter (Hz)

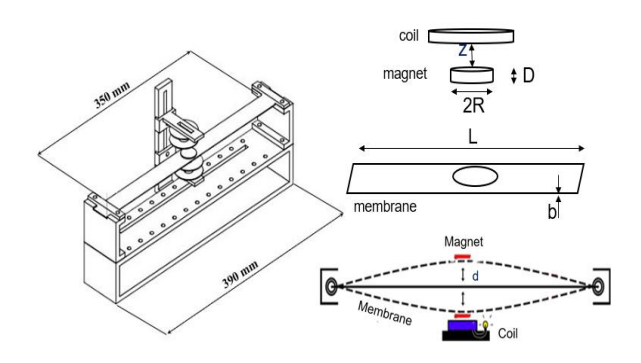


Fig. 1 View of the 350mm windbelt

- v : Wind speed (m/s)
- d : vibration amplitude of membrane during flutter (m)
- L : length of the membrane (m)
- b : thickness of the membrane (m)
- Br : Relative magnetic field strength for given magnet material (Tesla)
- D : Thickness of the cap magnet (m)
 R : Radius of the cap magnet (m)
- z : Distance between the pole and nearest conducting surface (m)

2.2 Experimental Setup

The experimental configuration is illustrated in Figure 2. The windbelt is placed in the test section of the subsonic wind tunnel. The inlet wind speed can be varied between 0 m/s and 20 m/s by changing the fan frequency of the wind tunnel. A high-speed camera is positioned horizontally next to the model in the wind tunnel to capture slow-motion video of the membrane vibration with a frame rate of up to 4000 fps. The equilibrium position of the magnet served as the reference point and is marked before testing. An image processing software is used to analyze the position of the magnet's center in each pixel of recorded video and then to determine the displacement of the magnet's center throughout 1 second of oscillation. The current and voltage generated by the windbelt go through the rectifier before being measured by using an Analog/Digital converter and registered directly on the connected computer.

2.3 Fluid-Structure Interaction Simulation (FSI)

The FSI problem is a combination of aerodynamics (CFD) and structural dynamics (CSD) problems. Once the aerodynamic and structural equations have been built, the

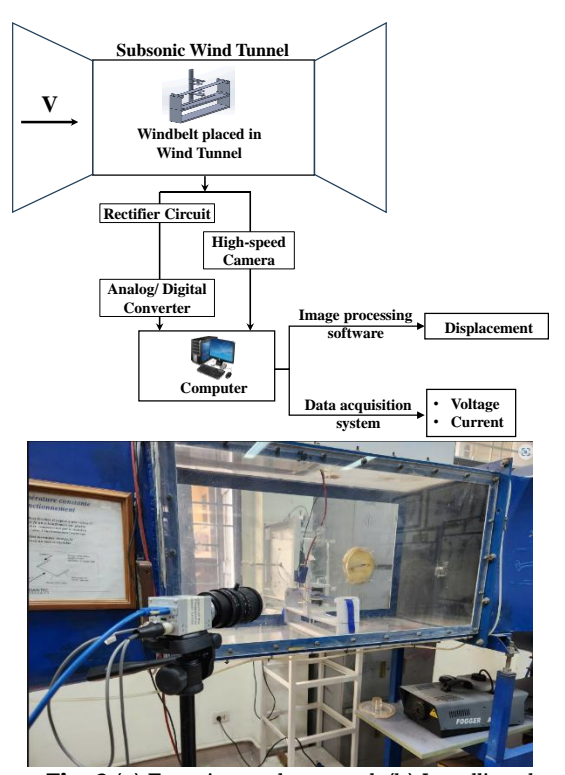


Fig. 2 (a) Experimental protocol; (b) Installing the windbelt in a wind tunnel

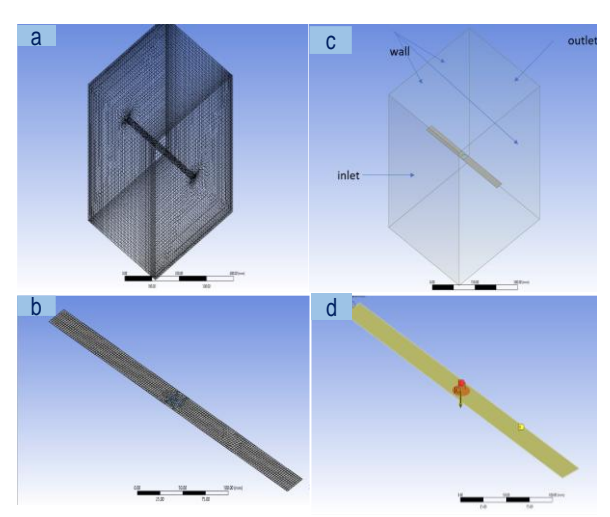


Fig. 3 (a) Meshing of aerodynamic envelope; (b) Conditions limite of CFD model; (c) meshing of the membrane; (d) FEA model of of the membrane

system of equations can be solved by specialized calculation software. One of them can be mentioned: the ANSYS Workbench. The 2-way FSI model is a continuous combination of fluid and mechanical structure. Results are transferred from fluid to mechanical structure and vice versa continuously throughout the calculation. For the two-way interaction problem, the iteration of the solution will be performed in both the fluid and structural solvers at each computational time step. Thus, the process of solving this problem is the implementation of the solution in each time step, and in that one-time step, there are separate solutions for the two problems of aerodynamics (fluent) and structural (structural).

The results of the two problems will be exchanged through the texture-fluid interaction region, and that result will become the solution condition for each problem in the next step. Specifically, the aerodynamic parameters will be calculated based on Fluent software; these parameters are transmitted through the interaction surface (the contact surface between the structural and fluid environments) and included to calculate the structural response (deformation, displacement) when subjected to aerodynamic forces at time step T. The change and deformation of the structure in this time step will change the interaction between the fluid, the structure, and the mesh of the substance liquid. This change will be propagated back to continue calculating the aerodynamic parameters in the next step $T+\Delta t$. This cycle continues until the end of the study period. The use of 2-way FSI simulation helps us to obtain the oscillation image of the magnet within 1 second of oscillation, from which the study can compare with the results obtained by the experiment.

The model was placed in an aerodynamic envelope with dimensions of 350x400x400 mm, a magnet diameter of 20 mm, and boundary conditions as shown in Figure 3(a&c). This domain aerodynamic envelope has a mesh size of 123044 hexa elements and 131516 nodes in Figure 3(a). The CFD model was built to calculate displacement and pressure on a membrane surface measuring 350x25x0.1 mm³. The mesh of the membrane consists of 1453 hexa elements and 11064 nodes as

Table 2Parameters of the material used to fabricate the membrane

Parameter	Value
Young's Module (GPa)	0.4309
Poisson Ratio	0.14
Density (kg/m³)	533.77

shown in Figure 3(b). The turbulent model used here is the k-w model with parameters Re = $2.0\times$ 10e5 where U = 100m/s is the velocity inlet. The kinematic viscosity is μ = 10 m/s with ρ = 10 kg/m³.

The FEA model was built to calculate the structure of the 350x25x0.1 mm³ membrane of the windbelt with two magnets attached. The film is made of canopy fabric, the properties of which are presented in Table 2. The magnets are considered to have a mass distribution with a mass of 0.01 kg (Figure 3d).

First, the modal analysis of the membrane-magnet structure is carried out to determine the specific oscillation frequency of the system. Then, based on the specific oscillation frequency parameter, the time step to set the calculation step for the FSI simulation will be calculated based on the formula $\Delta t = f/20$ in the study of (Slone *et al.*, 2004).

After verifying the accuracy of the simulation results compared to the experiment of the membrane with a length of 350 mm, the simulation models will be conducted with decreasing lengths from 350 mm to 198 mm to consider the effect of the wire length on the amplitude of oscillation.

3. Results and discussion

3.1 Natural frequency

Modal analysis is conducted with a magnet-attached membrane structure. The frequency and amplitude of the first mode of oscillation are shown in Figure 4. With this analysis, the oscillation frequency of mode 1 is f=0.1009 Hz, from which the corresponding time step is calculated to set for the 2-way FSI calculation.

3.2 Displacement of the membrane

The two-way FSI simulation results are calculated firstly with a membrane of 350mm length. The oscillation results through the measurement experiment by the image processing method are also processed to give a graph of the oscillation amplitude for each corresponding wind velocity.

Then, both qualitative and quantitative comparisons between the simulation and the experimental results of the vibrating membrane displacement were conducted at a wind speed of 3 m/s to evaluate the correctness of the simulation. Figure 5 (a&b) shows the oscillation mode image of the vibrating

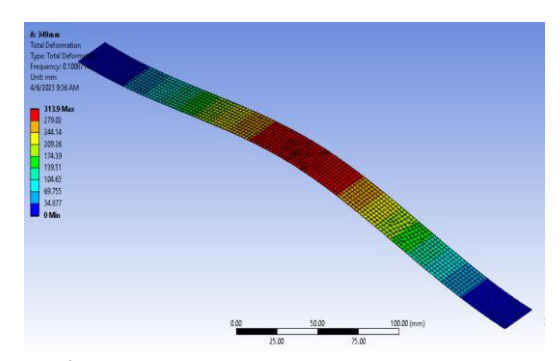


Fig. 4 The first mode of membrane vibration.

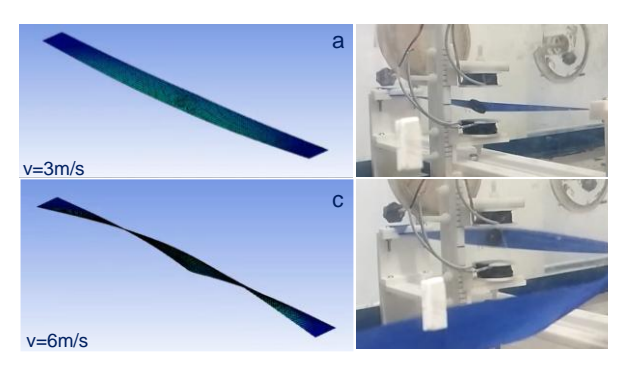


Fig. 5 (a) The oscillation mode at 3 m/s in simulation; (b) The oscillation mode at 3 m/s in experiment; (c) The oscillation mode at 6 m/s in simulation; (d) The oscillation mode at 6 m/s in experiment

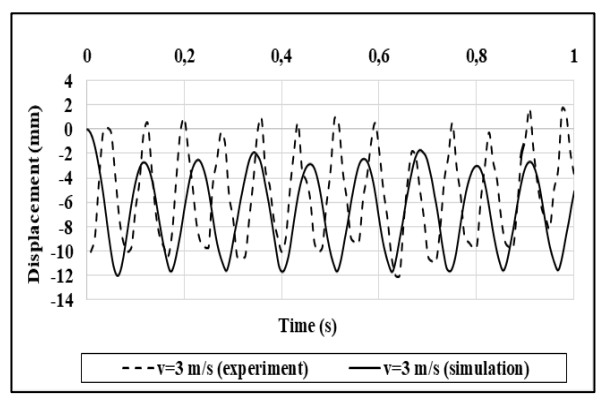


Fig. 6 (a) Membrane displacement at 3 m/s in simulation); (b) Membrane displacement at 3 m/s in experiment)

membrane at a wind velocity of 3 m/s in simulation and in experiment. These photos show that the oscillation mode in the 2-dimensional FSI simulation is similar to the experimental image.

Figure 6 shows the results of displacement amplitude at the magnet placement using both numerical simulation and experimental methods. The amplitude and frequency of the oscillation over time between simulation and experiment show a relatively small deviation. The maximum amplitude in the simulation is 11.99 mm, a deviation of 0.51% from the experimental value.

The two-dimensional FSI simulation results are calculated at five inlet wind velocity values of 2.5, 3, 4, 5, and 6 m/s. The results of displacement measurements at different velocities are shown in Table 3. The membrane will have a negative tendency

 Table 3

 The largest displacement between simulation and experiment

The largest displacement between simulation and experiment				
Velocity (m/s)	Maximum	Maximum	Error	
	displacement	displacement	compared	
	magnitude	magnitude	with	
	(simulation)	(experiment)	experiment	
	(mm)	(mm)	(%)	
2.5	12.05	11.32	6.48	
3	11.99	12.06	0.51	
4	11.74	11.00	6.72	
5	11.51	10.75	4.77	
6	9.72	10.68	8.98	

0.1

2

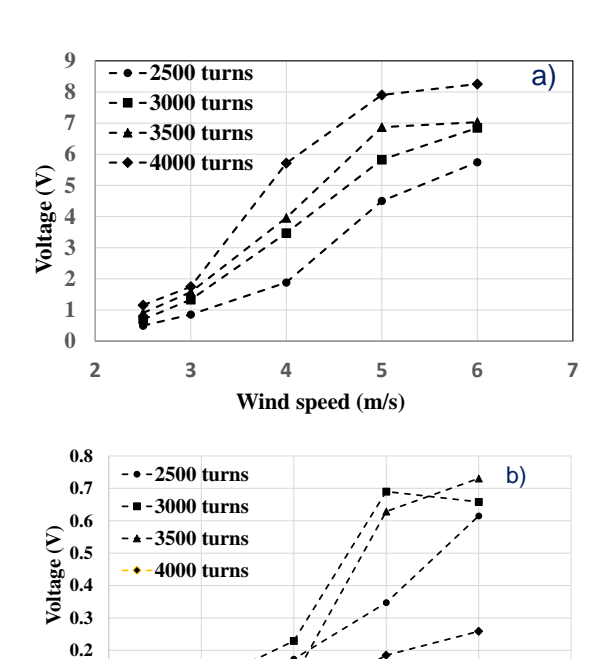


Fig. 7 (a) No-load voltage of each loop according to wind speed; (b) Load voltage of each turn according to wind speed

Wind speed (m/s)

6

7

to oscillate due to the gravitational force generated by the magnet's mass. At a velocity of 3 m/s, the deviation between the simulated amplitude and displacement is the smallest and about 0.51%. When the wind speed increases to 6 m/s, this deviation is at most about 9%. As the experimental wind speed continues to increase as well as the simulation, the error will be even greater because the oscillation of the membrane is no longer in a single mode but is an overlapping combination of many modes as shown in Figure 5(c&d).

3.3 Experimental result of voltage and power

The measurement of the voltage and current according to the method mentioned in paragraph 2.2 is carried out for a windbetl with a length of 350 mm. The no-load voltage of the windbelt is measured at 2500, 3000, and 4000 spins in the 2.5 to 6 m/s speed range by three experiments, and the findings are shown in Figure 7(a).

When comparing at the maximum wind speed of 6 m/s, it can be observed that the open-circuit voltage increases from below 6 V to over 8 V (approximately 33%). This trend is fully consistent with the results reported in the studies of (Fernandez *et al.*, 2018) and (Le *et al.*, 2023). The magnitude of the open-circuit voltage in this case ranges from 8 V to 12 V (Table1). The voltage generated increases as the number of coil turns rises.

As can be seen from the graph, the output voltage of the generator tends to increase proportionally with the number of turns of the copper coil. The larger the number of turns, the higher the voltage output. By doing five measurements of voltage measurement with a load in the speed range of 2.5 to 6 m/s, with a load of 1000 Ω resistance and windings of 2500, 3000, 3500, and 4000 turns, respectively, the following findings were obtained in Figure 7(b).

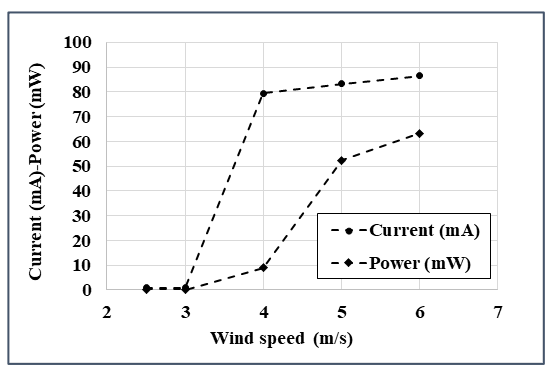


Fig. 8 Current and power according to wind speed

Compared to previous studies on generator voltage under load conditions using the flutter phenomenon, a significant voltage drop is observed when a load is applied. At a wind speed of 2.5 m/s, this drop can be nearly tenfold. For instance, in the study by (Vu $\it et al., 2021$), a larger windbelt (L \times W = 0.62 m \times 0.02 m) generated 8.7 V under open-circuit conditions, which decreased to 1.1 V when a load was connected at the same wind speed.

Since the power generated at wind speeds of 2.5 and 3 m/s is minimal and below the critical threshold, it gradually increases as the wind speed approaches 4 m/s, eventually reaching a peak value of 63.24 mW at 6 m/s, as shown in Figure 8. Compared with the power output of generators operating on the same principle, as summarized in Table 1, several observations can be made. Firstly, the maximum power output of this generator is 63.24 mW at a wind speed of 6 m/s. This value is comparable in magnitude to the generator developed by (Angelo et al., 2017), recognizing that power output also depends on factors such as the size of the fluttering membrane and the number of coil turns; however, in terms of order of magnitude, the results are consistent. Secondly, (Pimentel et al. ,2010) achieved a higher power output of 171 mW, attributed to operation at a significantly higher wind speed of 20 m/s. Lastly, at lower wind speeds of 2–3 m/s, the generator with a 350 mm wire in this study produced very low power, whereas under similar wind conditions, but with a 620 mm wire, the windbelt generated 0.39 mW as reported by (Le et al., 2023).

3.4 Influences of membrane length on the output voltage and power.

Based on the results of the simulation of the oscillation amplitude of the vibrating membrane according to the velocity and the theoretical formula in section 2, the potential difference can be calculated through the ratio f=v/d, where v is the inlet wind velocity and d is the oscillation amplitude of the belt membrane. With L=350 mm, B=0.017 Tesla, v=3 m/s, d=11.99 mm, b=1 mm, and N=3000 rounds, the theoretical voltage calculated by theory is 1.6 V, taking into account the voltage drops. This value, compared to the U=1.331 V experiment, has a deviation of 16.9%. This error is acceptable.

The membrane simulation models were conducted with different lengths decreasing by about 20 mm, including 350 mm, 321 mm, 297 mm, 270 mm, 248 mm, 224 mm, and 198 mm. The 2-way FSI simulation in Figure 9 shows the displacement-time graphs of the samples as their lengths are gradually reduced from the initial length of 350 mm. In the initial case, it is evident that at L = 321 mm, the oscillation occurs at the same frequency with only a slightly smaller amplitude compared to that of the original length L = 350 mm. As the belt length continues to

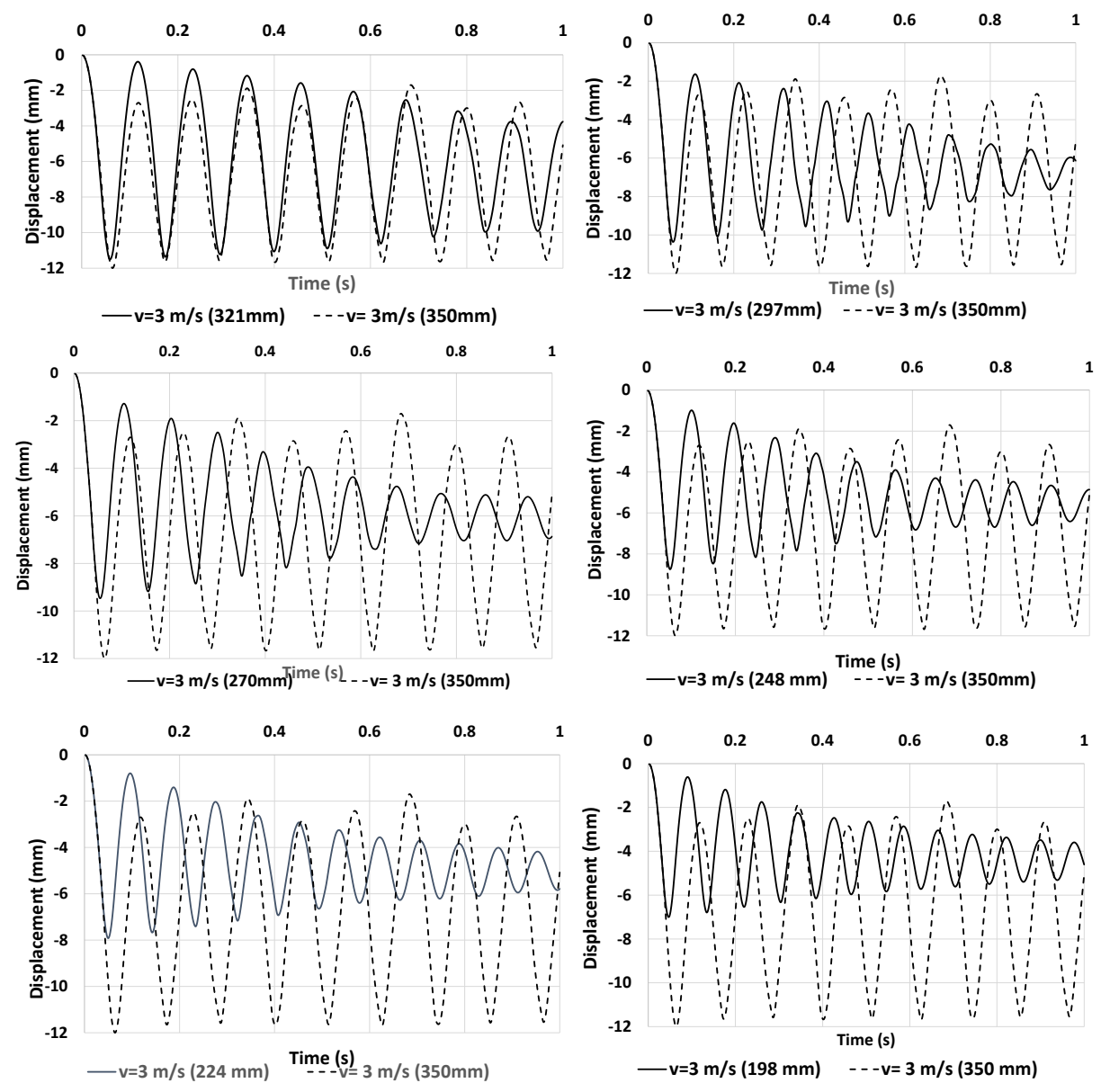


Fig. 9 Displacement at the center of the magnet with a membrane length of 350mm, 321mm, 297mm, 270mm, 248mm, 224mm and 198mm

decrease, the amplitude also diminishes, and the damping trend of the oscillation becomes increasingly evident.

It can be observed that with shorter membrane lengths, the oscillation amplitude decreases, while the oscillation frequency remains stable. Additionally, as the membrane length is reduced, the oscillation changes from damped at shorter lengths to harmonic at a length of 350 mm, as illustrated in Figure 9.

The maximum displacement is defined as the difference between the highest and lowest displacements of the magnet's center over one second of oscillation. As shown in Figure 10, the displacement tends to increase with both longer rope lengths and higher wind speeds. The oscillation amplitude of the vibrating membrane with a length of 198 mm is the smallest, measuring 7 mm, and remains relatively constant as wind velocity increases. For a length of 224 mm, the amplitude remains fairly stable at wind speeds below 5 m/s. However, at 6 m/s, all membranes exhibit a sharp increase in amplitude. At wind speeds of 5 m/s or higher, as shown in Figure 5(c), the oscillation transitions from a single mode to a combination of

multiple modes, resulting in larger but more unstable amplitude variations.

The instability of oscillation amplitude at wind speeds of 5 m/s or higher directly affects the theoretically calculated potential difference for different wire lengths. As shown in Figure 11(a), at wind speeds of 2.5 m/s, 3 m/s, and 4 m/s, the potential difference generated decreases progressively with shorter wire lengths. This occurs because the potential difference (U) depends on the ratio of velocity (v) to displacement (d); as v decreases, d also decreases, leading to a lower U. However, at higher wind speeds of 5 m/s and 6 m/s, fluctuations in the measured voltage difference across membranes of different lengths are observed. This can be attributed to the mixing of oscillation modes when wind speed exceeds the 5 m/s threshold. Notably, the shortest belt length of 198 mm achieves the highest voltage output of 6 V at the maximum wind speed of 6 m/s, and voltage generation is only observed starting from a wind speed of 3 m/s. When considering the influence of belt membrane displacement on voltage and power output, (Vu et al., 2021) observed at a wind

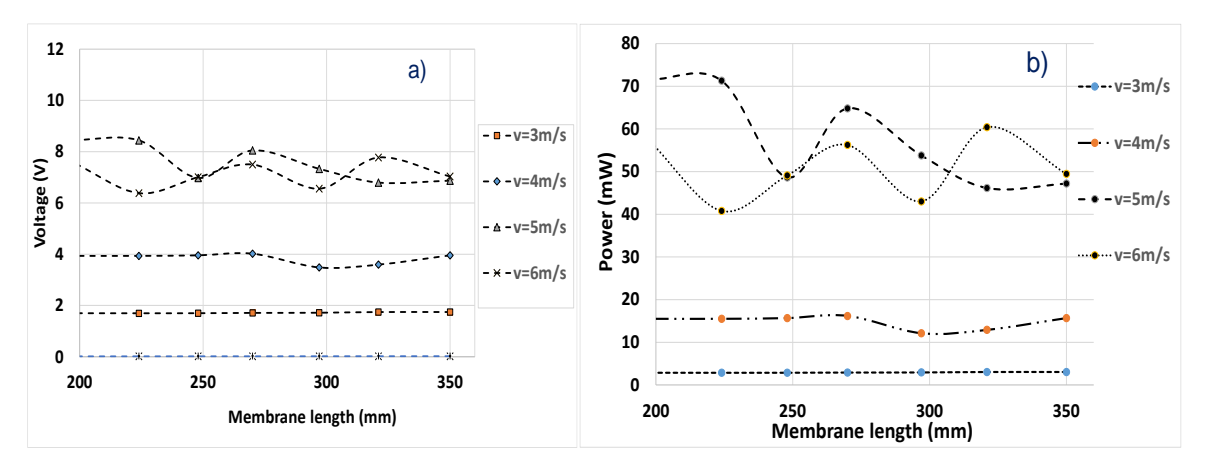


Fig. 11 a) No load Voltage for different lengths of membrane. b) Power calculates with $R=1000\Omega$ for different lengths of membrane

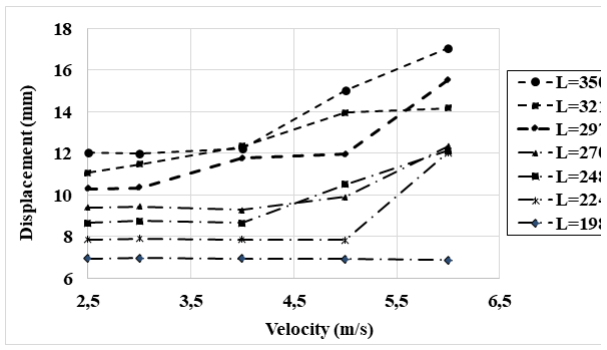


Fig. 10 Displacement of the membrane in function of wind speed.

speed of 2.5 m/s that for belts with greater lengths (500 mm–600 mm), the voltage increased with longer wire lengths and larger oscillation amplitudes. In the case of shorter belts, as studied in this research (200–300 mm), it can be seen that at lower wind speeds of 3 m/s and 4 m/s, the variation in voltage under changing oscillation amplitudes is minimal. This is because the voltage and power output values are too small for the changes to be clearly noticeable. At higher wind speeds, such as 5 m/s and 6 m/s, there are slight fluctuations in both voltage and power output due to the emergence of combined oscillation modes.

However, in reality, with wire lengths shorter than 300 mm, when a load is connected and a voltage drop occurs, the power values for the current device are very low and unmeasurable. Using theoretical calculations with a 1000Ω load, the corresponding power generated from this no-load voltage at different belt membrane lengths is shown in Figure 11(b). At a speed of 3 m/s, the generated power is approximately 2.8 mW and does not vary with length. At a speed of 4 m/s, this power reaches a maximum of 16 mW. For speeds of 5 m/s and 6 m/s, the signal exhibits some fluctuation, with the minimum power around 40 mW and the maximum around 70 mW. Specifically, with the shortest wire length of 198 mm, the generator can achieve a power range from 2.8 mW to 56.9 mW. With the aim type of small-scale generator to applying this telecommunication towers equipped with pressure and temperature sensors—where the protective casings of these sensors typically range in size from 200 cm to 300 cm—windbelt lengths between 200 mm and 350 mm have been considered. The idea is to utilize the sensor's protective casing as housing for the generator, allowing it to supply power directly to the sensor and replace lithium batteries (3V, 30 mAh). In this context, windbelts with a length of 200 mm can meet the required power range.

4. Conclusion

Renewable energy is an extremely essential development direction, so research on wind power-based generators is a possible development direction in the future. Especially small generator devices will replace the use of batteries, which cause huge pollution in the environment. Moreover, the use of numerical simulation tools helps us save costs instead of conducting experiments.

In this study, with the goal of determining the power output and voltage of a wind belt with the shortest possible wire length (fixed width of 20 mm), several key findings have been identified. First, the amplitude measurement method of flutter compared to FSI simulation at a velocity of 3 m/s showed a maximum deviation of 9%, indicating a high level of agreement between FSI simulation and actual experimentation. Next, the theoretical voltage based on simulated oscillation amplitude and the directly measured voltage had a maximum difference of 12%, showing that the theoretical calculation method combined with FSI simulation reasonably predicts the device's voltage. Lastly, concerning the power generation capability of the device depending on wire length, the maximum power output achieved with L=350 mm was 8V in the no-load case and 0.8V with R=1k Ω load. With the minimum wire length of 198mm, the measured no-load voltage was 7.5 V, while no power could be measured under load as it was nearly zero. Additionally, within the velocity range of 2-6 m/s, at speeds below 3 m/s, almost no current could be measured, and at speeds above 5 m/s, the oscillation signal became unstable due to multiple oscillation modes overlapping. The device performs best at a velocity of 3

The theoretical calculations based on the measured oscillation amplitude of the belt membrane allow for the estimation of the power output of a short 198 mm belt to range from 2.8 mW to 56.9 mW. This demonstrates the feasibility of using this device as a replacement for battery power sources in stress sensors installed on utility poles and telecommunication towers.

In the future, research can be developed by substituting factors that affect membrane vibrations, such as changing the length of the membrane, changing the number of magnets on the membrane, and changing the angle of attack of the membrane. In particular, research will focus on designing sensor enclosures capable of generating and storing electricity to power the sensors, aiming to eliminate the need for battery replacement on these poles.

Acknowledgements

This study is funded by Hanoi University of Science and Technology (HUST) under grant number T2023-PC-017. The authors are also grateful for the cooperation between Viettel Aerospace Institute and Hanoi University of Science for their support of this research.

References

- Abdehvand, M.Z., Roknizadeh, S.A.S., Hamid, M.S. (2021). Modeling and analysis of novel coupled magneto-electro-aeroelastic continuous system for flutter-based energy harvesting system. *Energy*, 230, 120742. https://doi.org/10.1016/j.energy.2021.120742
- Abderrahmane, H.A., Pai doussis, M.P., Fayed, M., Ng, H.D. (2012). Nonlinear Dynamics of Silk and Mylar Flags Flapping in Axial Flow, J. *Wind Eng. Ind. Aerodyn*, 107–108 ,225–236. https://doi.org/10.1016/j.jweia.2012.04.021
- Ali, A., Ali, S., Shaukat, H., Khalid, E., Behram, L., Rani, H., Altabey, W.A., Kouritem, S.A., Noori, M. (2024). Advancements in piezoelectric wind energy harvesting: A review, Results in Engineering 21, 101777. https://doi.org/10.1016/j.rineng.2024.101777
- Allen, J. J., Smits, A.J. (2001). Energy harvesting eel. *Journal of Fluids and Structures* 15, 629-640. https://doi.org/10.1006/jfls.2000.0355
- Angelo, I. A., Calautit, J.K., Hughes, B,R. (2017) Integration of aeroelastic belt into the built environment for low-energy wind harnessing: Current status and a case study. *Energy Conversion* and *Management* 149, 830-850. https://doi.org/10.1016/j.enconman.2017.03.030.
- Angelo, I. A., Calautit, J.K., Hughes, B.R. (2017) Evaluation of the integration of the Wind-Induced Flutter Energy Harvester (WIFEH) into the built environment: Experimental and numerical analysis, Applied Energy 207, 61-77. https://doi.org/10.1016/j.apenergy.2017.06.041
- Bae, J., Lee, J., Kim, S.M., Ha, J., Lee, B.S., Park, Y.J., Choong, C., Kim, J.B., Wang, Z.L., Kim, H.Y., Park, J.J., Chung, U.I. (2014). Flutter-driven triboelectrification for harvesting wind energy. *Nature communications*. https://doi.org/10.1038/ncomms5929
- Bangi, V.K.T., Chaudhary, Y., Guduru, R.K., Aung, K.T and Reddy, G.N. (2017). Preliminary investigation on generation of electricity using micro wind turbines placed on a car. *Int. Journal of Renewable Energy Development*, 6(1), 75-81, https://doi.org/10.14710/ijred.6.1.75-81
- Başkut. E., Akgül, A. (2012). Development of a Closely Coupled Procedure for Dynamic Aeroelastic Analyses. *Scientific Technical Review* 62(2), 30-39. https://api.semanticscholar.org/CorpusID:232719271
- Buyukkseskin, I., Tekin, S. A., Gurel, S., Genc, M S. (2019) Electricity Production from Wind Energy By Piezoelectric Material. International Journal of Renewable Energy Development, 8(1), 41-46. https://doi.org/10.14710/ijred.8.1.41-46
- Calautit, K., Cameron, J. (2023). State-of-the-art review of micro to small-scale wind energy harvesting technologies for building integration. *Energy Conversion and Management*, 20, 100457, https://doi.org/10.1016/j.ecmx.2023.100457
- Chawdhury S, Morgenthal G. (2018). Numerical simulations of aeroelastic instabilities to optimize the performance of flutter-based electromagnetic energy harvesters. *J Intell Mater Syst Struct*, 29(4), 479- 95. https://doi.org/10.1177/1045389X17711784

- De Sousa, VC., Junior, D.C. (2015), Airfoil-based piezoelectric energy harvesting by exploiting the pseudoelastic hysteresis of shape memory alloy springs. *Smart Master Struct, 24*(12). https://iopscience.iop.org/article/10.1088/0964-1726/23/12/125014
- Erturk, A., Vieira, A. W. G. R., Marqui, C. D., Inman, D. J. (2010). On the energy harvesting potential of piezo aeroelastic systems. *Applied physics letters 96*, 184103. https://doi.org/10.1063/1.3427405
- Fei, F., Mai, J.D., Li, W.J. (2012). A wind-flutter energy converter for powering wireless sensors. Sensors and Actuators A 173, 163–171. doi: 10.1016/j.sna.2011.06.015
- Fernandez, E., Gobres, E., Thio-ac, A.C., Jandumon, M.S., Ong, C.L.G., Perez, R.B., Ramos, P.G. (2018). Design Optimization of low power windbelt electric generator using Piezoelectric Transducer. *IEEE 10th International Conference on Humanoid, Nanotechnology, Information Technology, Communication and Control, Environment and Management (HNICEM)*, 1–6. https://doi.org/10.1109/HNICEM.2018.8666404
- Hasan, M., EI-Shahat, A., Rahman, M. (2017). Performance investigation of three combined airfoils blades small scale horizontal axis wind turbine by FEM and CFD analysis. *Journal of Power and Energy Engineering*, 05(05), 14-27. https://doi.org/10.4236/jpee.2017.55002
- Heo, Y.G., Choi, N.J., Choi, K.H., Ji, H.S., Kim, K.C. (2016). CFD study on aerodynamic power output of a 110 kW building augmented wind turbine. *Energy and Buildings*, 110-kW62-73. https://doi.org/10.1016/j.enbuild.2016.08.004
- Kan, J., Liao, Wang, W.J., Wang, Yan, S.M., Jiang, Y., Zhang, Z. (2021) Enhanced piezoelectric wind-induced vibration energy harvester via the interplay between cylindrical shell and diamond-shaped baffle, *Nano Energy*, 89(B), 106466. https://doi.org/10.1016/j.nanoen.2021.106466.
- Keshavarzi, M.M., Yousefi-Komab, A., Nejatc, A., Mohtasebi, S.S. (2016). Comparison of Two-Way Fluid-Structure Interaction Simulation of a Wing in Transonic Inviscid Flow for Structured and Unstructured Grid. 6th International Conference on Acoustics & Vibration.
 - https://www.researchgate.net/publication/308364860
- Kurhade, S.A., Kanhe, S.S., Khaparkar, A.A. (2017). Aeroelastic Flutter Energy Harvesting, *International Research Journal of Engineering and Technology (IRJET)*, 04(01), 1752-1754. https://www.irjet.net/archives/V4/i1/IRJET-V4I1350.pdf
- Lang, T., Wang, Gao, H.H., Wang, R., Tao, T., Xu, J. (2025).

 Experimental investigation on vortex-induced vibration characteristics of the dual parallel suspenders. *Engineering Structures*, 322, 119075. https://doi.org/10.1016/j.engstruct.2024.119075
- Le, T.T.N., Vu, D.Q., Luu, T.T., Vu, D.Q. (2023). Experimental Investigation of the Vibration Amplitude of the Belt Membrane on the Output Power of a Small Windbelt Generator. *Journal of Aeronautics, Astronautics and Aviation* 55(3S), 539 546. https://doi.org/10.6125/JoAAA.202309_55(3S).04
- Lu, Z., Wen, Q., He, X., Wen, Z. (2019). A Flutter-Based Electromagnetic Wind Energy Harvester: Theory and Experiments. *Appl. Sci.*, 9(22), 4823, https://doi.org/10.3390/app9224823
- Perez, M., Boisseau., S., Gasnier, P., Willemin, J., Reboud, J.L. (2015)
 An electret-based aeroelastic flutter energy harvester. *Smart Mater. Struct.* 24, 035004, https://doi.org/10.1088/0964-1726/24/3/035004.
- Phan, H., Shin, D.M., Jeona, S.H., Kanga, T.Y., Han, P., Kim, G.H., Kim, H.K., Kima, K., Hwang, Y.H., Hong, S.W. (2017). Aerodynamic and aeroelastic flutters driven triboelectric nanogenerators for harvesting broadband airflow energy. *Nano Energy 33*, 476-484. https://doi.org/10.1016/j.nanoen.2017.02.005
- Pimentel, D., Musilek, P., Knight, A., Heckenbergerova, J. (2010). Characterization of a wind flutter generator, 9th International Conference on Environment and Electrical Engineering (EEEIC), Prague, Czech Republic, 81–84, doi: 10.1109/EEEIC.2010.5490015.
- Salmon, F., Chatellier, L. (2021). 3D fluid–structure interaction simulation of a hydrofoil at low Reynolds number. *Journal of Fluids and Structures*, 111, 103573. https://doi.org/10.1016/j.jfluidstructs.2022.103573

- Shaikh, F.K., Zeadally, S. (2016) Energy harvesting in wireless sensor networks: A comprehensive review. *Renew. Sustain. Energy Rev.*, 55, 1041–1054. https://doi.org/10.1016/j.rser.2015.11.010
- Shan X., Tian H., Cao H., Feng J., Xie T. (2020). Experimental Investigation on a Novel Airfoil-Based Piezoelectric Energy Harvester for Aeroelastic Vibration, *Micromachines* 11, 725. https://doi.org/10.3390/mi11080725
- Shawn, F., 2004, Generator utilizing fluid-induced oscillations, Patent US2008129254 (A1), Humdinger wind energy.
- Shuguang Li, S., Yuan, J., Lipson, H. (2011). Ambient wind energy harvesting using crossflow fluttering. *Journal of applied physics*, 109(2), 026104 026104-3. https://doi.org/10.1063/1.3525045.
- Sirohi, J., Mahadik, R. (2011). Harvesting Wind Energy Using a Galloping Piezoelectric Beam. *Journal of Vibration and Acoustics*, 134(1), 011009. https://doi.org/10.1115/1.4004674
- Slone, A.K., Pericleous, K., Bailey, C., Cross, M., Bennett, C. (2003) A finite volume unstructured mesh approach to dynamic fluid-structure interaction: an assessment of the challenge of predicting the onset of flutter. *Applied Mathematical Modelling*, 28(2), 211-239. https://doi.org/10.1016/S0307-904X(03)00142-2
- Tathode, P.S., Phapale, M., Teli, P., Lomte, P., Bute, P. (2017) Generation of Clean Energy using Concept of Wind Belt. International Journal of Engineering Research & Technology, 5(5), 792-798. https://api.semanticscholar.org/CorpusID:55784594
- Vinayan, V.A., Yap, T. C., Go, Y.I. (2019). Design of Aeroelastic Wind Belt for Low-Energy Wind Harvesting. *IOP Conference Series: Earth and Environmental Science* 268, 012069. https://doi.org/10.1088/1755-1315/268/1/012069
- Vu, D. Q., Nguyen, V. S., Dinh, T. H., Vu, Q.H. (2016). Wind tunnel and initial field tests of a micro generator powered by fluid-induced

- flutter. Energy for Sustainable Development 33, 75-83. https://doi.org/10.1016/j.esd.2016.04.003
- Vu, D.Q., Le, T. T.N., Luu, T. T. (2021). Experimental Study of a Small-Capacity Wind-Powered Generator Based on Aeroelasticity Phenomenon, *Advances in Asian Mechanism and Machine Science* 113, 961-970. https://link.springer.com/chapter/10.1007%2F978-3-030-91892-7_92
- Wu, Z., Luo, G., Yang, Z., Guo, Y., Li, K., Xue, Y. (2022). A comprehensive review on deep learning approaches in wind forecasting applications. CAAi Trans Intell Technol, 7(2), 129-143. https://doi.org/10.1049/cit2.12076
- Yates, E. C., Land, N. S., Foughner, J. T. (1963). Measured and calculated subsonic and transonic flutter characteristics of a 45 sweptback wing planform in air and in freon-12 in the Langley transonic dynamics tunnel. *National Aeronautics and Space Administration Technical Note* D-1616.
- Yates, E., Carson, Jr. (1987). AGARD standard configuration for dynamic response, candidate configuration I.-Wing 445.6, National Aeronautics and Space Administration Technical Note TM 100492
- Zakaria, N.M., Zulkifli, M.S., Mukhtar, A. (2023). The Potential of Flutter-Based Windbelt for Energy Generation in Low Wind-Speed Regions: A Case Study in Malaysia. *Journal of Advanced Research in Fluid Mechanics and Thermal Sciences*, 107(1), 125-141. https://doi.org/10.37934/arfmts.107.1.125141
- Zhang C., He XF., Li SY., Cheng YQ., Rao Y.A. (2015). A wind energy powered wireless temperature sensor node, *Sensors 15(3)*, 5020-5031. https://doi.org/10.3390/s150305020



© 2025. The Author(s). This article is an open access article distributed under the terms and conditions of the Creative Commons Attribution-ShareAlike 4.0 (CC BY-SA) International License (http://creativecommons.org/licenses/by-sa/4.0/)